ANALYSIS OF THE SHEAR CAPACITY OF HIGH-STRENGTH PRESTRESSED SCC BEAMS USING DIGITAL IMAGE CORRELATION (DIC) AND FEM

Kristof De Wilder, Department of Civil Engineering, KU Leuven, Belgium

Guido De Roeck, PhD, Department of Civil Engineering, KU Leuven, Belgium

Lucie Vandewalle, PhD, Department of Civil Engineering, KU Leuven, Belgium

ABSTRACT

Despite more than a century of research effort, the problem of determining the shear capacity of a structural concrete member remains open for dispute. In this work, partial results of six prestressed I-shaped SCC beams with and without shear reinforcement subjected to a four-point bending test until failure are reported. The main investigated parameters are the amount of prestressing, the amount of shear reinforcement and the shear span-to-depth ratio respectively. During four of the six specimens, full-field three-dimensional displacements were discretely measured in both zones where a shear force occurs using two stereo vision digital image correlation (DIC) systems. Together with the experimentally observed failure load and mode, these displacement data were used to validate numerical finite element models (FEM). A good correlation was found between the experimentally observed and numerically predicted data. Based on the numerical output, an investigation of the mechanical behaviour is made. It was found that a significant portion of the applied shear force is carried in both upper and lower flanges. These contributions however are usually neglected in current codes of practice (i.e. Eurocode 2).

Keywords: prestressed concrete, shear, finite element modeling, mechanical behaviour

INTRODUCTION

After more than a century of research effort, shear remains an area within the scientific community where disagreement remains amongst researchers. From the early days of concrete construction, engineers have sought for models that accurately determine the shear resistance of a structural concrete member. In the earliest contributions, Ritter [1] idealized the flow of forces within a structural concrete member by means of a truss model, as shown in Fig. 1. The top and bottom chord resist the applied bending moment whereas the combination of inclined compressive struts and vertical tension ties resist the applied shear force. Important progress has been made in the last fifty years when, under the influence of the theory of plasticity, the truss model was extended and systematized. This model is easy to understand and is still the basis for current international codes of practice [2-4].

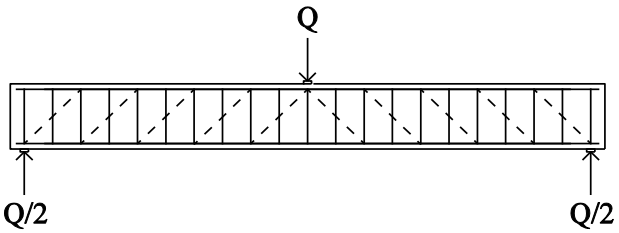

Fig. 1. Truss model concept (compressive struts in dashed lines; vertical tension ties in full lines)

Although the aforementioned truss model is highly didactic and easy to understand, it remains a (semi-)empirical design approach and thus not suitable for the entire spectrum of structural concrete members loaded in shear. Therefore, from the last thirty years onwards, research focus has shifted from (semi)-empirical design approaches towards more rational theoretical models based on equilibrium [5-8] and compatibility [9-11] conditions. These theories are based on the actual mechanical behaviour of structural concrete members loaded in shear. The aforementioned models however, are mainly intended for reinforced concrete rather than prestressed concrete and despite the large research effort, our understanding of shear in structural concrete members remains incomplete [12].

This paper aims to make a contribution to a better understanding of the mechanical behaviour of prestressed concrete beams failing in shear by reporting the preliminary results of six tests. In the first part of this paper, the specimen properties, experimental setup and the observed structural behaviour will be reported. A comparison between the experimental results and analytical predictions using current codes of practice (i.e. Eurocode 2 [2, 13]) will be made. In the second part of this paper, the experimental data will be used to validate numerical predictions obtained from nonlinear finite element models (FEM). A good correlation was found between the experimentally observed data and the numerical predictions concerning failure load, failure mode and displacements. Finally, an investigation of the shear carrying mechanisms is made based on the FEM output.

EXPERIMENTAL INVESTIGATION

SPECIMEN DESIGN

In this study, the preliminary results of six prestressed concrete I-shaped beams are reported. Each specimen is labeled with the descriptive letter B followed by a number ranging from 101 to 106. Each specimen is 7000mm (23.0 ft.) long, 630mm (24.8 in.) high and has a flange width equal to 240mm (9.5 in.). The web of each specimen is 70mm (2.8 in.) wide. All beams are provided with eight 7-wire strands at the bottom with a nominal diameter of 12.5mm (0.5 in.) and two 7-wire strands at the top with a nominal diameter of 9.3mm (3/8 in.). Shear reinforcement, consisting of single-legged stirrups with a nominal diameter of 6mm (0.24 in.) and a center-to-center distance equal to 150mm (5.9 in.), is provided for all beams except specimen B103 and B106. At both ends of each specimen, splitting reinforcement is provided with a nominal diameter of 8mm (0.32 in.) and a center-to-center distance equal to 50mm (2 in.) The geometry and prestressing layout of all specimens is shown in Fig. 2.

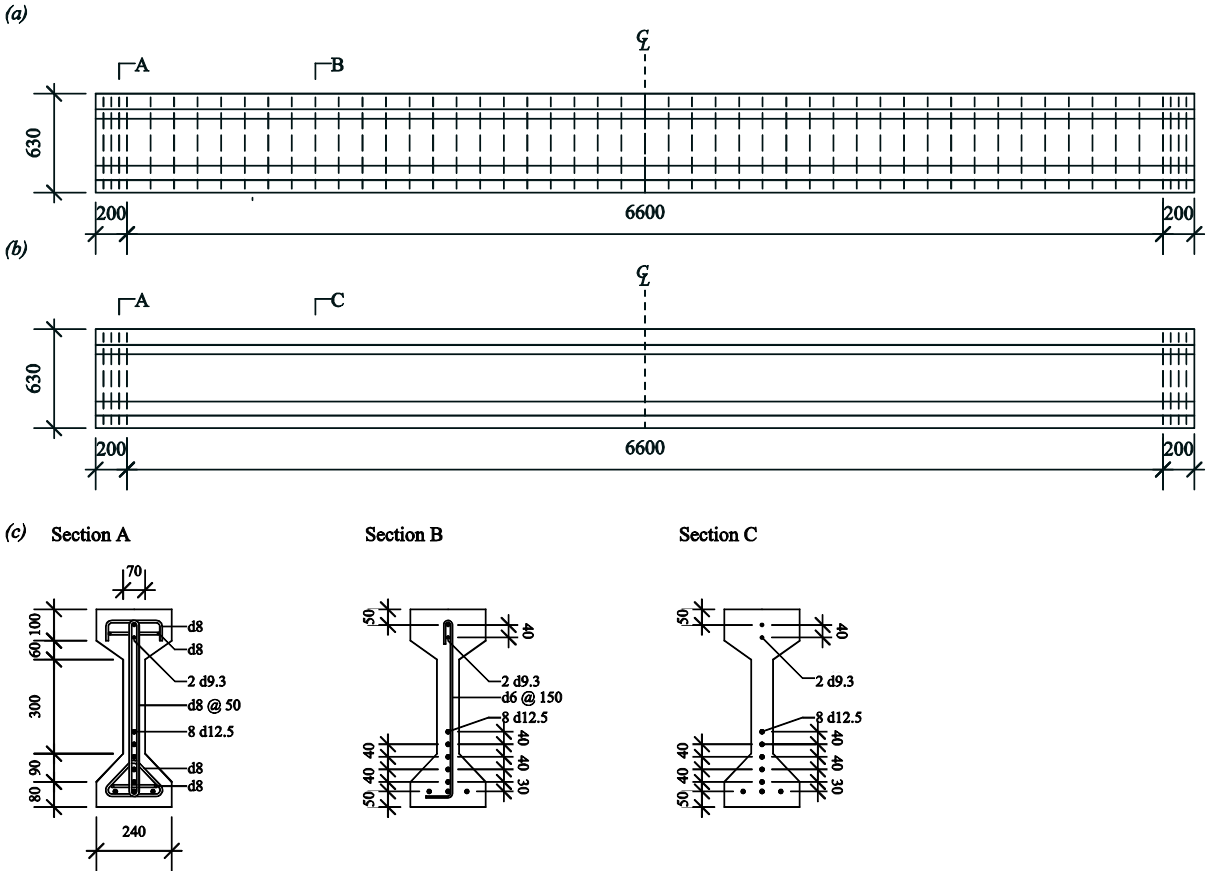

Fig. 2 (a) geometry, prestress and reinforcing layout of specimens B101, B102, B104 and B105; (b) geometry, prestress and reinforcing layout of specimens B103 and B106; (c) cross sections of specimens and reinforcement details; note: units in millimeter (25.4mm = 1 in.)

MATERIALS

The concrete mixture was designed to have a characteristic cylindrical compressive strength equal to 50MPa (7252 psi). Cement was specified as CEM I 52.5 R ANN, whereas the coarse aggregate consisted of a 12mm (0.5 in.) maximum size gravel. Limestone filler and a high-range water reducer were also provided. The concrete batch weights are listed in Table 1.

Material	Amount
CEM I 52.5R ANN, kg/m³ (lb/yd³)	380.0 (640.5)
gravel 2/12, kg/m³ (lb/yd³)	1097.5 (1849.9)
sand 0/2, kg/m³ (lb/yd³)	684.5 (1153.8)
water, kg/m³ (lb/yd³)	225.0 379.3)
limestone filler, kg/m³ (lb/yd³)	150.0 (252.8)
high-range water reducer, l/m³ (oz/yd³)	10.7 (197.2)

Table 1. Concrete mixture batch weights

Tensile tests were performed on the shear and splitting reinforcement to determine the modulus of elasticity E_s, , the yield and ultimate stress, f_{ym} respectively f_{tm}, and the strain at failure ε_u. The same characteristics of the prestressing strands were taken from the manufacturer. The results are summarized in Table 2.

Type	d_p, d_s^*	E_s	f_{ym}	f_{tm}	ε_u
	mm (in.)	GPa (ksi)	MPa (ksi)	MPa (ksi)	%
top prestressing reinforcement					
7-wire	9.3 (0.38)	198 (28717)	1737 (252)	1930 (280)	5.20
bottom prestressing reinforcement					
7-wire	12.5 (0.5)	198 (28717)	1737 (252)	1930 (280)	5.20
shear reinforcement					
cold worked	6 (0.24)	203 (29443)	608 (88)	636 (92)	2.73
splitting reinforcement					
cold worked	8 (0.32)	203 (29443)	542 (79)	603 (88)	5.97

note: * nominal diameter of prestressing (subscript *p*) or conventional (subscript *s*) reinforcement

Table 2. Reinforcement properties

SPECIMEN CONSTRUCTION

Concrete mixtures were made in volumes of 2m³ (2.6 yd³). Each test specimen consists of just one mixture. Together with each specimen, concrete cubes (sides 150mm [5.9 in.]), cylinders (height 300mm [11.8 in.]; diameter 150mm [5.9 in.]) and prisms (length 600mm [23.6 in.]; sides 150mm [5.9 in.]) were cast to determine the mean compressive strength f_{cm} based on cylinders, the mean compressive strength $f_{cm,cube}$ based on cubes, the mean secant modulus of elasticity E_{cm} and the flexural tensile strength $f_{ctm,fl}$. A summary of the results per specimen is shown in Table 3. All beams were cast into steel formwork which was removed in less than 24 hours after casting. The day after casting, demountable mechanical strain gauge points (DEMEC-points) were glued onto one of the side surfaces over 2000mm (78.7 in.) to allow the determination of the immediate and time-dependent stress losses in the prestressing reinforcement.

Each prestressing strand was tensioned the day prior to casting. The strand force was measured using a pressure transducer installed on the hydraulic jack. Each strand of specimens B101-B103 was given an initial prestrain equal to 7.5mS (σ_{m0} = 1488MPa [215.8 ksi]) whereas each strand of specimens B104-B106 was given an initial prestrain equal to 3.8mS (σ_{m0} = 750MPa [108.8 ksi]). While it is uncommon in the industry to reduce stress levels below the allowable, the stresses were varied to isolate the effect of varying the prestressing force while keeping the longitudinal reinforcement ratio constant. At the day of testing, it was found that the stress losses in the bottom and top prestressing reinforcement were approximately equal to 25% respectively 10% of the initial stress level.

Specimen	f_{cm}, MPa (ksi) [#*]	$f_{cm,cube}$, MPa (ksi) [#*,s**(s***)]	E_{cm}, GPa (ksi) [#*]	$f_{ctm,fl}$, MPa (psi) [#*]
B101	74.5 (10.8) [2]	81.8 (11.9) [3, 1.0 (0.2)]	n.a.	6.4 (928.2) [2]
B102	71.8 (10.4) [2]	87.1 (12.6) [3, 6.3 (0.9)]	44.5 (6454) [2]	6.0 (870.2) [2]
B103	95.0 (13.8) [1]	94.9 (13.8) [2]	41.1 (5961) [1]	5.1 (739.7) [2]
B104	92.9 (13.5) [2]	74.3 (10.8) [3, 11.6 (1.7)]	47.9 (6947) [2]	6.6 (957.2) [2]
B105	90.3 (13.1) [2]	87.3 (12.7) [3, 10.9 (1.6)]	40.6 (5888) [2]	5.3 (768.7) [2]
B106	83.6 (12.1) [2]	86.9 (12.6) [3, 5.1 (0.7)]	42.2 (6120) [2]	7.6 (1102.3) [2]

note: *: number of tested specimens; ** standard deviation, MPa; *** standard deviation, ksi
n.a.: not applicable

Table 3. Concrete mixture properties

EXPERIMENTAL SETUP

All specimens are subjected to a four point bending test, as shown in Fig. 3(a). The test are carried out in load-control using a hydraulic press (Instron, maximum capacity of 2.5 MN [562 kip]). The force from the hydraulic press is converted to two point loads by means of a steel construction profile (HEB 400) lying on two steel bearing cylinders. The total load is monotonically increased at 0.250kN/s (56.2lb/s), i.e. applied shear force rate equal to 0.125kN/s (28.1 lb/s), until failure occurs. The distance between the support points is equal to 5000mm (16.4 ft.) . The distance outside the support points is therefore equal to 1000mm (3.3 ft.) at each end. This setup firstly enables the authors to study shear outside the length needed for the prestressing force to gradually develop over the member's height and secondly to prevent failure due to debonding of the longitudinal reinforcement. The shear span *a*, refer to Fig 3(a), is equal to 1600mm (5.3 ft.) for specimens B101 and B104 and 2000mm (6.6 ft.) for beams B102-B103 and B105-B106. An overview of the investigated properties of each beam is given in Table 4.

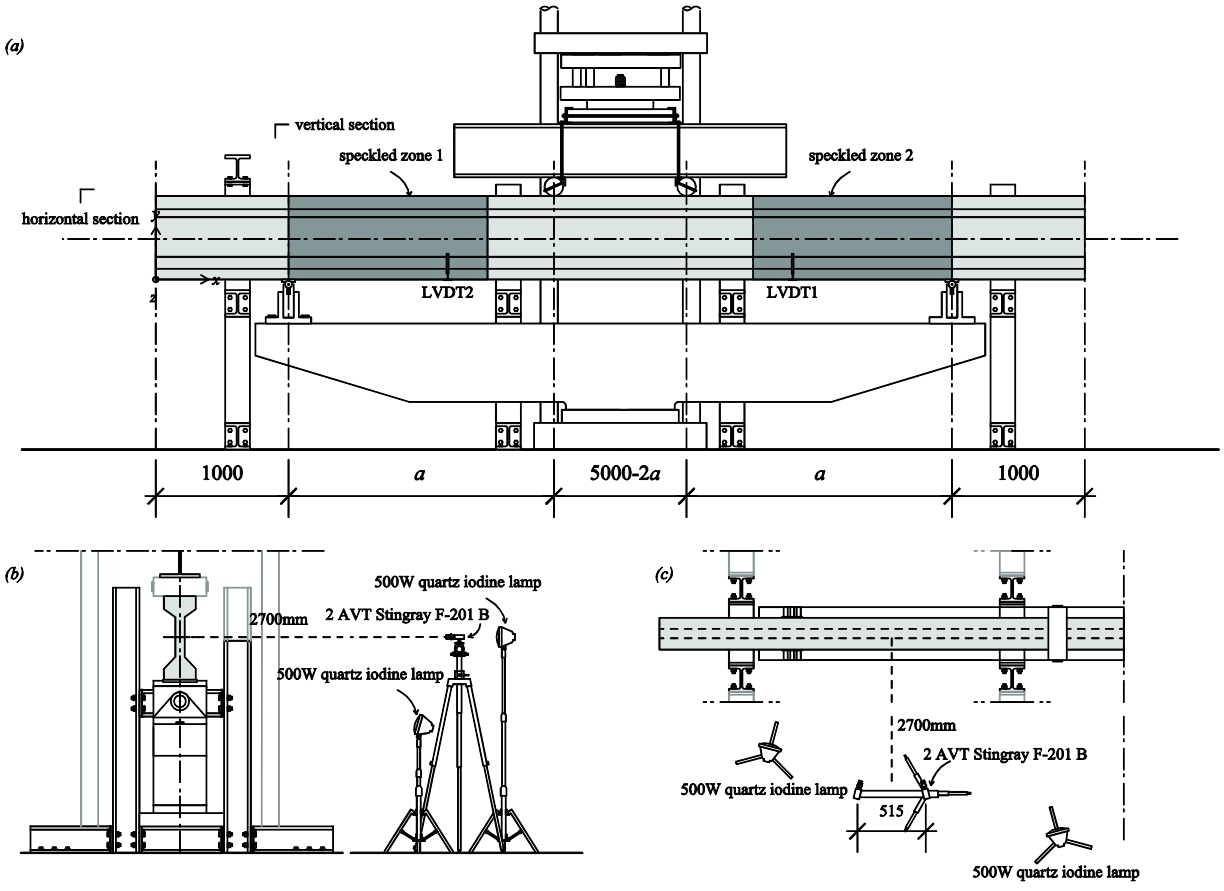

Fig. 3. Experimental setup: (a) front view of experimental setup with indication of speckled zones (units in millimeter, 25.4mm = 1 in.); (b) vertical section of experimental setup (units in millimeter) and (c) horizontal section of experimental setup (units in millimeter)

Specimen	σ_{m0}	a	$\rho_w = A_{sw}/(b_w s)^*$
	MPa (ksi)	mm (ft.)	mm²/mm² (=in.²/in.²)
B101	1488 (215.8)	1600 (5.3)	0.0027
B102	1488 (215.8)	2000 (6.6)	0.0027
B103	1488 (215.8)	2000 (6.6)	0
B104	750 (108.8)	1600 (5.3)	0.0027
B105	750 (108.8)	2000 (6.6)	0.0027
B106	750 (108.8)	2000 (6.6)	0

note: $^*A_{sw}$: area of shear reinforcement; s: center-to-center distance of shear reinforcement

Table 4. Overview of investigated parameters per specimen

Apart from two linear variable differential transformers (LVDTs), refer to Fig. 3(a), full-field three-dimensional displacements were measured using the digital image correlation (DIC) technique for specimens B103-B106. As an optical full-field measurement technique, DIC has proven to be an ideal tool for a wide range of applications, including the identification of the mechanical material behaviour through inverse modeling [14, 15], structural health monitoring [16] and the study of the deformation characteristics of a wide range of materials [17-19]. The basic principle behind this technique is to calculate the displacements on the surface of an object by taking images of a random speckle pattern in the undeformed and deformed state. There are three main steps in the DIC method: (1) capture images, (2) correlation process and (3) post-processing phase.

In the reported study, both zones where a shear force occurs, refer to Fig. 3(a), were investigated using two stereo-vision DIC systems. Each zone under investigation measures approximately 1500mm by 630mm. Each system consists of two charge-coupled device (CCD) 8-bit cameras (AVT Stingray F-201B; 1628 pixels by 1236 pixels resolution) with lenses having a focal length equal to 12mm mounted on a tripod. The cameras are located at a perpendicular distance equal to 2700mm (8.9 ft.) from the specimen under investigation, refer to Fig. 3(b)-(c). To ensure good lighting conditions and small exposure times, two 500W quartz iodine lamps are provided per investigated zone as shown in Fig. 3(b)-(c). The image acquisition rate of each camera is equal to 2Hz with an exposure time of 20ms. All images of the four cameras are synchronized with the analog data of the hydraulic press (i.e. applied load and corresponding displacement of the press head). In this contribution, a subset based method is applied to correlate two speckle patterns. This method considers a pixel and its neighborhood in the undeformed image f and searches the same subset in the deformed image g by adopting a maximization routine for a similarity function. The formalism is clearly explained in [20]. In this study, maximization of the similarity function is obtained by adopting the zero-normalized sum of squared differences (ZNSSD) routine. The size of the subset can be chosen as desired prior to the evaluation. In this work, the dimensions of each subset were 27 by 27 pixels where each pixel has the physical dimension of approximately 1mm (0.04 in.). Reproducibility of the speckle pattern is ensured by applying the same pattern onto each beam by using a stencil printing technique [21].

The correlation process and the post-processing of the data are done using MatchID 3D [20]. During the post-processing phase, strains are calculated by smoothing the measured displacement data over a certain zone to damp out the effect of noise and local uncertainties. This is a commonly adopted method [22]. Here, strains are averaged over 51 by 51 displacement data points. Taking into account the step size of 3 pixels and the physical dimension of one pixel, this means that strains are averaged over approximately 150 by 150mm (5.9 by 5.9 in.). This relatively large base length is justified when dealing with heterogeneous materials which exhibit a profound cracking pattern. For this setup, the standard deviation s of the in-plane horizontal U (x-axis) and vertical V (y-axis) displacement, refer to Fig. 3(a), are found to be equal to 21µm (8.3 10^{-4} in.) and 11µm (4.3 10^{-4} in.) respectively. The standard deviation of the out-of-plane displacement W (z-axis) is an order of magnitude higher, equal to 155 µm (6.1 10^{-3} in.), but also less important for the reported experiments since primarily in-plane displacements and deformations will occur. The standard deviation of the horizontal ε_{xx}, vertical ε_{yy} and shear strain ε_{xy} is found to be equal to 112µS, 241µS and 140µS respectively.

STRUCTURAL BEHAVIOUR

In this section, the experimentally observed structural behaviour is reported. Fig. 4(a)-(f) show the measured load-displacement response curves for all investigated specimens. From Fig. 4(c), it can be seen that specimen B103 remains nearly perfectly linear elastic until failure. Since no shear reinforcement is provided, no redistribution of internal forces is possible after the occurrence of the first diagonal crack. The overall structural behaviour of specimen B106 deviates from perfectly linear elastic behaviour until failure due to the occurrence of bending cracks prior to the first diagonal crack leading to sudden failure. Specimens B101-B102 and B104-B105 exhibit a profound post-cracking behaviour until failure is reached. Table 5 summarizes the experimentally observed shear failure load and failure mode for each specimen. The experimental failure load can be compared to analytical predictions using the shear strength provisions found in Eurocode 2 (EC2) [2, 13]. According to EC2, the shear strength of a member with shear reinforcement is given by Eq. (1). Eq. (2) or (3) should be used to determine the sectional shear strength of a structural concrete member without shear reinforcement in a section which is uncracked respectively cracked due to bending (i.e. cracks starting from the bottom fiber of the beam).

$$V_R = V_{R,s} = \frac{A_{sw}}{s} z f_{yw} \left(cot(\theta) + cot(\alpha)\right) sin(\alpha) \leq \frac{\alpha_{cw} \nu_1 f_{cm} b_w z \left(cot(\theta) + cot(\alpha)\right)}{\left(1 + cot^2(\theta)\right)} \quad (1)$$

$$V_R = V_{R,c} = \frac{I b_w}{S} \sqrt{\left(f_{ct}\right)^2 + \alpha_l \sigma_{cp} f_{ct}} \quad (2)$$

$$V_R = V_{R,c} = \left[0.18k\left(100\rho_l f_{cm}\right)^{1/3} + 0.15\sigma_{cp}\right] b_w d \geq \left(0.035k^{\frac{3}{2}} f_{cm}^{\frac{1}{2}} + 0.15\sigma_{cp}\right) b_w d \quad (3)$$

In the previous equations, A_{sw}/s denotes the area of shear reinforcement per unit length; z is the internal lever arm; f_{yw} is the yield stress of the shear reinforcement; θ denotes the angle between the horizontal and the concrete compressive struts; α_{cw} is a coefficient taking into account the state of stress in the compression chord; ν_1 is a strength reduction factor for cracked concrete; f_{cm} is the average cylindrical compressive strength; b_w denotes the web width; α is the angle between the horizontal and axis of the shear reinforcement; I denotes the second moment of area; S is the first moment of area above and about the centroidal axis; f_{ct} is the concrete tensile strength; α_l is a factor taking into account the bond characteristics; σ_{cp} represents the average compressive stress due to a normal force, i.e. prestressing force; k is a factor accounting for the size effect in shear; ρ_l denotes the geometrical longitudinal reinforcement ratio; and d is the member's effective depth.

In the aforementioned equations, average material strength properties and no partial safety factors were used to better estimate the actual failure load. The results of these calculations are also incorporated into Table 5. From these results, three preliminary conclusions can be drawn: (1) firstly, it can be seen that increasing the prestressing force while keeping the longitudinal reinforcement ratio constant, increases the shear capacity for specimens with (B101-B104 and B102-B105) and without (B103-B106) shear reinforcement. This effect however is neglected in the shear strength provisions of EC2 for concrete members with shear reinforcement.

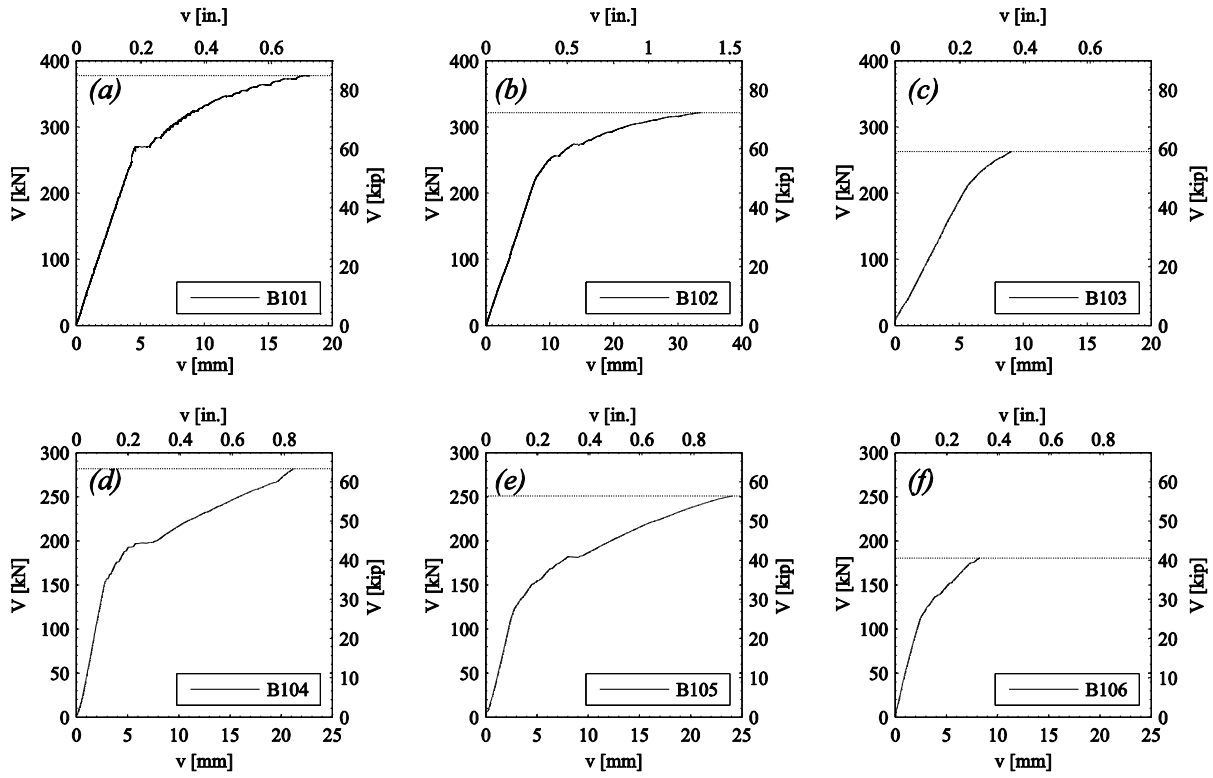

Fig. 4. Load-displacement response curves determined at 1200mm (3.94 ft.) from support point for specimens B101, B103-B106 and 2000mm (6.56 ft.) for specimen B102

Specimen	Experiment		Eurocode 2 [2, 13]		
	Failure load $V_{u,exp}$, kN (kip)	Failure mode	Failure load $V_{u,pred}$, kN (kip)	$V_{u,exp}/V_{u,pred}$	Failure mode
B101	377.7 (84.9)	DC*	165.4 (37.2)	2.28	DT
B102	321.6 (72.3)	DT**	165.4 (37.2)	1.94	DT
B103	262.8 (59.1)	DT	264.2 (59.4)	1.00	DT
B104	281.8 (63.4)	DT	139.5 (31.4)	2.02	DT
B105	251.2 (56.5)	DT	139.5 (31.4)	1.80	DT
B106	179.7 (40.4)	DT	87.0 (19.6)	2.07	DT

note: *DC: failure due to diagonal compression (crushing of concrete struts); **DT: failure due to diagonal tension (yielding and rupture of shear reinforcement)

Table 5. Failure load and mode properties, failure load predictions according to EC2

(2) Secondly, it can be noted that EC2 predicts the correct failure mode for all specimens except for specimen B101. (3) Finally, it can be concluded from Table 5 that EC2 severely underestimates the shear capacity of all specimens with shear reinforcement and beam B106 without shear reinforcement. A good estimate of the shear capacity is found for specimen B103. However, since the aforementioned beam remains nearly perfectly linear elastic until failure, it can be expected that the linear-elastic expression, given by Eq. (2), yields accurate results.

FINITE ELEMENT MODEL ANALYSIS

FINITE ELEMENT MODEL DEVELOPMENT

In order to further investigate the discrepancy between experimental results and analytical predictions as reported in Table 5, a three-dimensional nonlinear finite element model is constructed of all specimens with shear reinforcement using the commercially available software package ANSYS v14. Due to double symmetry of the geometry and loading conditions, this model is reduced to a quarter of each specimen minimizing computational effort. The concrete matrix is modeled using hexahedron elements with eight nodes and linear shape functions. Each node has three translational degrees of freedom. Both longitudinal and shear reinforcement types are discretely modeled using truss elements. Experimentally determined material characteristics, as reported in Table 2 and Table 3, were used to define materials models for both concrete and reinforcement. To model failure of the concrete matrix in tension and compression and to account for multiaxial conditions on the uniaxial stress-strain behaviour, failure envelopes as proposed by [23] are adopted. Similar to the experiments, the simulations are carried out in load-control.

FINITE ELEMENT MODEL VALIDATION

The ability of the FEM to reconstruct the experiment is validated by firstly assessing the numerically predicted failure load and mode. The results are summarized in Table 6. From Table 6 it can be seen that a good correlation is found between the experimentally observed and numerically predicted failure load. The failure mode is correctly predicted for all specimens except for beam B101. Fig. 5(a)-(d) show the experimentally observed cracking pattern at failure and the location of the shear reinforcement.

Specimen	Experiment		FEM		
	Failure load $V_{u,exp}$, kN (kip)	Failure mode	Failure load $V_{u,pred}$, kN (kip)	$V_{u,exp}/V_{u,pred}$	Failure mode
B101	377.7 (84.9)	DC*	355.6	1.06	DT
B102	321.6 (72.3)	DT**	316.3	1.02	DT
B104	281.8 (63.4)	DT	274.5	1.03	DT
B105	251.2 (56.5)	DT	258.0	0.97	DT

note: *DC: diagonal compression failure; **DT: diagonal tension failure

Table 6. Comparison between experimental and numerical failure load and mode

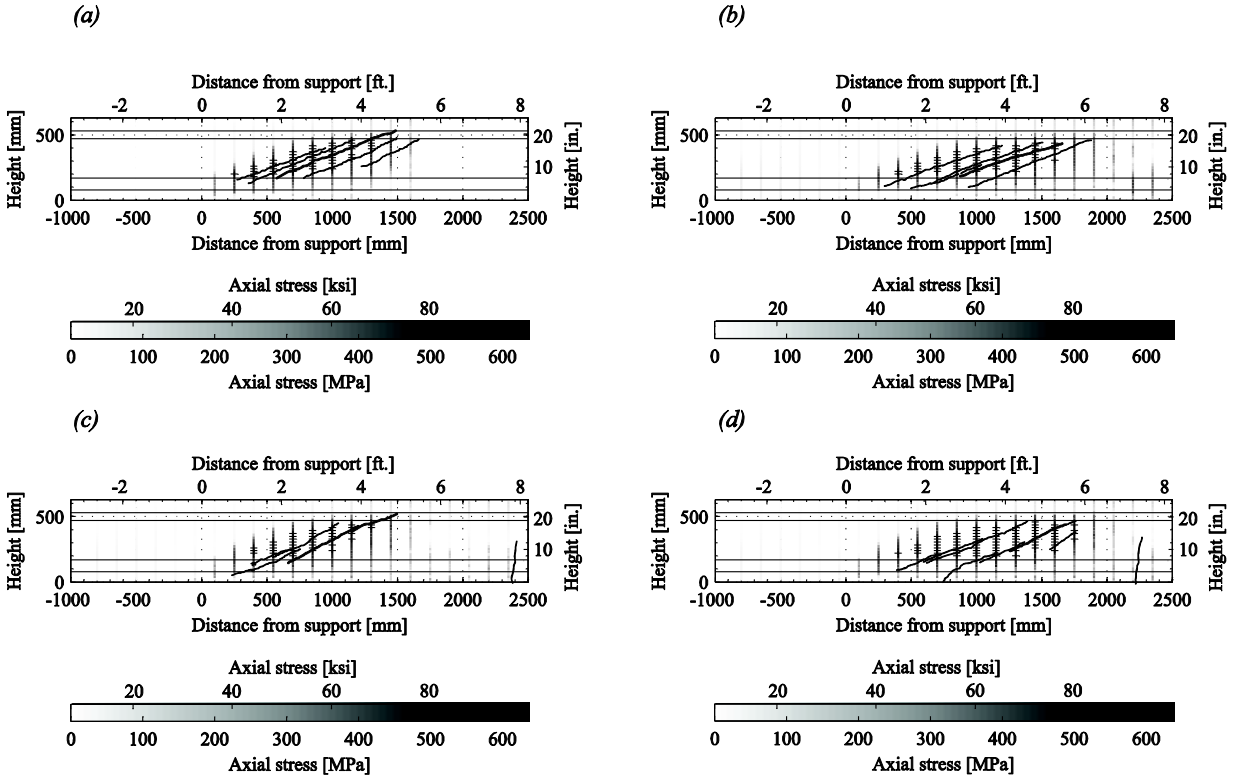

Fig. 5. Cracking pattern at failure, location and axial stress level of shear reinforcement at the numerically predicted failure load ('+' indicates location where yield stress is exceeded) (a) B101; (b) B102; (c) B104; (d) B105

Note that only the side where failure occurred, is shown in the aforementioned Fig. 5(a)-(d). The grey value of each reinforcement element represents the numerically predicted axial stress level at failure. These stress levels correspond well with the location and angle of the cracking pattern.

Finally, the finite element model output can be validated by comparing the experimentally observed and the numerically predicted displacement data, both in the time and space domain. In Fig. 6(a)-(d), both the numerical and experimental load-displacement response curves, as reported earlier in Fig. 4(a)-(b) and Fig. 4(d)-(e), are shown. Fig. 7(a)-(d) show the experimental and numerical horizontal and vertical displacements for specimen B104 at 95% of the experimentally observed failure. Similar results were found for other specimens. From Fig. 6(a)-(d) and Fig. 7(a)-(d), it can be concluded that the numerical model is capable of reconstructing the nonlinear behaviour due to cracking of the concrete matrix and subsequent yielding of the reinforcement.

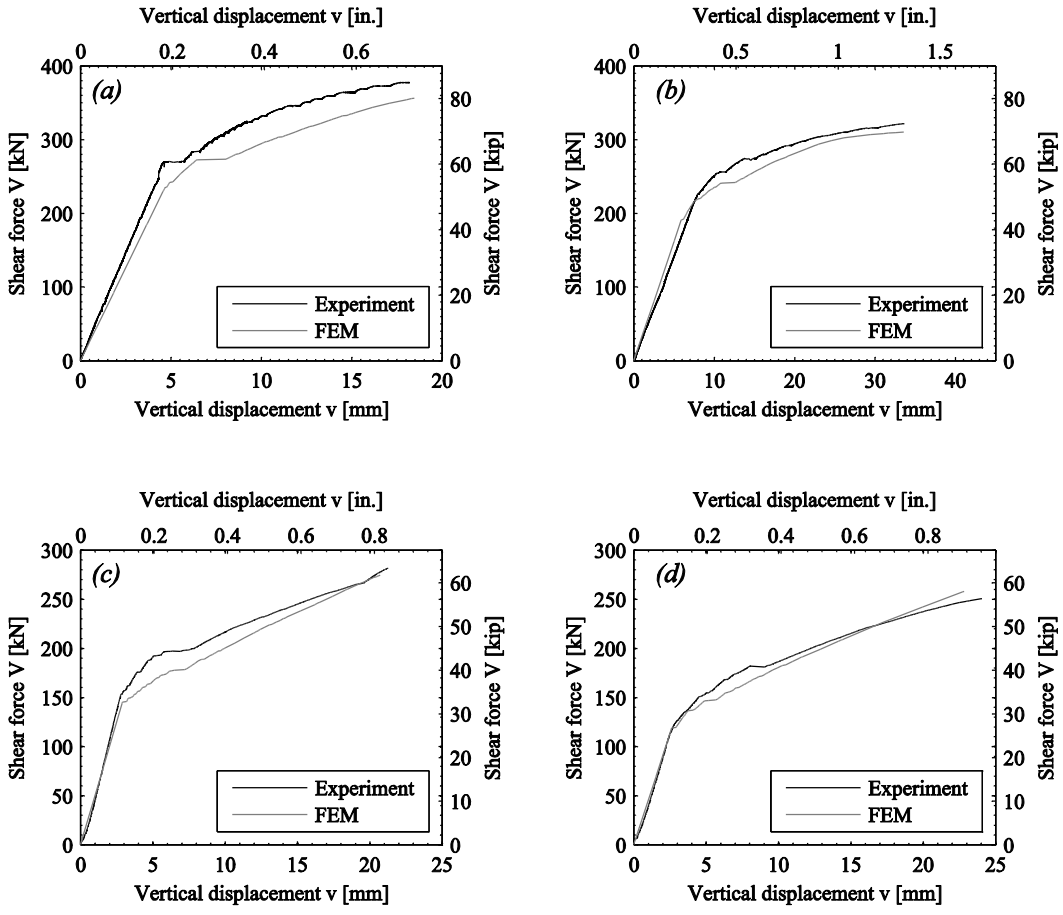

Fig. 6. Comparison between experimental and numerical load-displacement response curves: (a) specimen B101; (b) specimen B102; (c) specimen B104; (d) specimen B105

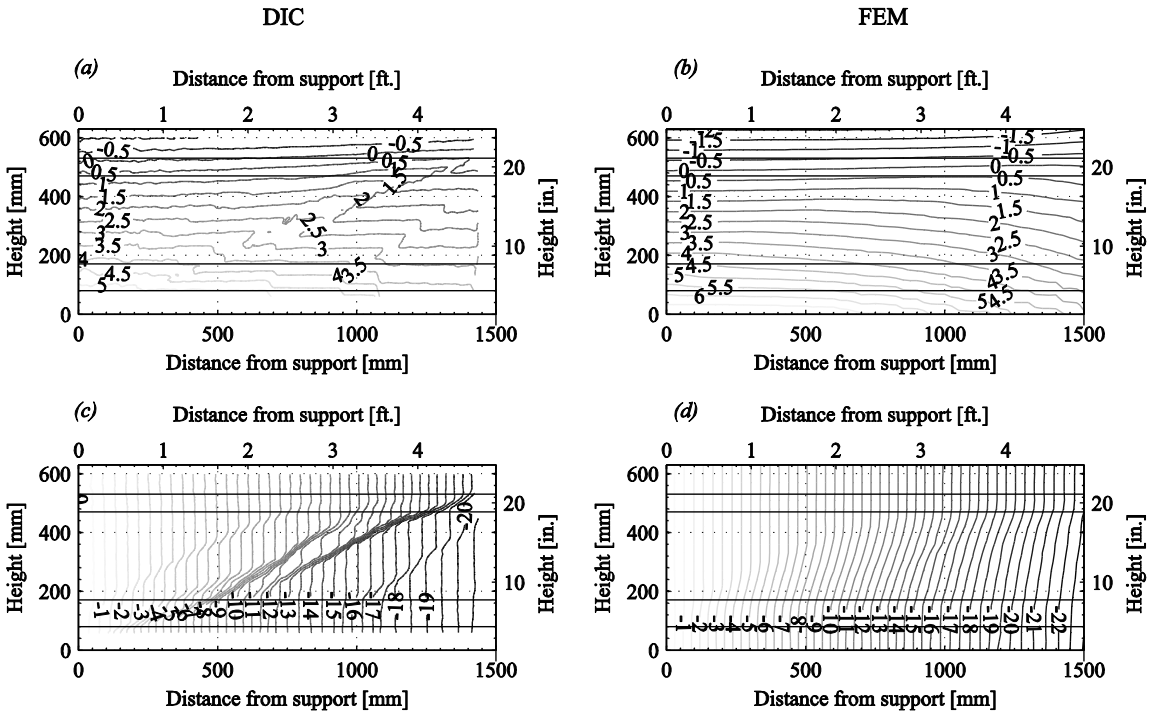

Fig. 7. Contour plot of experimental (a,c) and numerical (b,d) horizontal (a,b) and vertical (c,d) displacements for specimen B104 at 95% of the experimentally observed failure load as a function of the horizontal and vertical coordinate (note: 25.4mm = 1in.)

ANALYSIS OF RESULTS AND DISCUSSION

In Fig. 8, the experimentally observed and numerically predicted angle θ of specimen B104, measured between the horizontal and the principal compressive strain direction vector, is plotted as a function of the distance from the support point and the applied load level. In Fig. 8(a) and Fig. 8(b) this aforementioned angle is determined at a height equal to 382mm (15.0 in.) respectively 272mm (10.7 in.) from the bottom of the beam. Both height coordinates lie within the web of the beam. It is assumed that the direction of the principal compressive strain coincides with the direction of the principal compressive stress. This assumption is also made by other researchers [9, 24]. Secondly, it is also assumed that the principal compressive strain direction on the surface of the beam is the same as the principal compressive strain direction at the location of the shear reinforcement within the beam. The experimentally observed and numerically predicted angle θ is compared to the minimum allowable angle according to EC2 [2, 13].

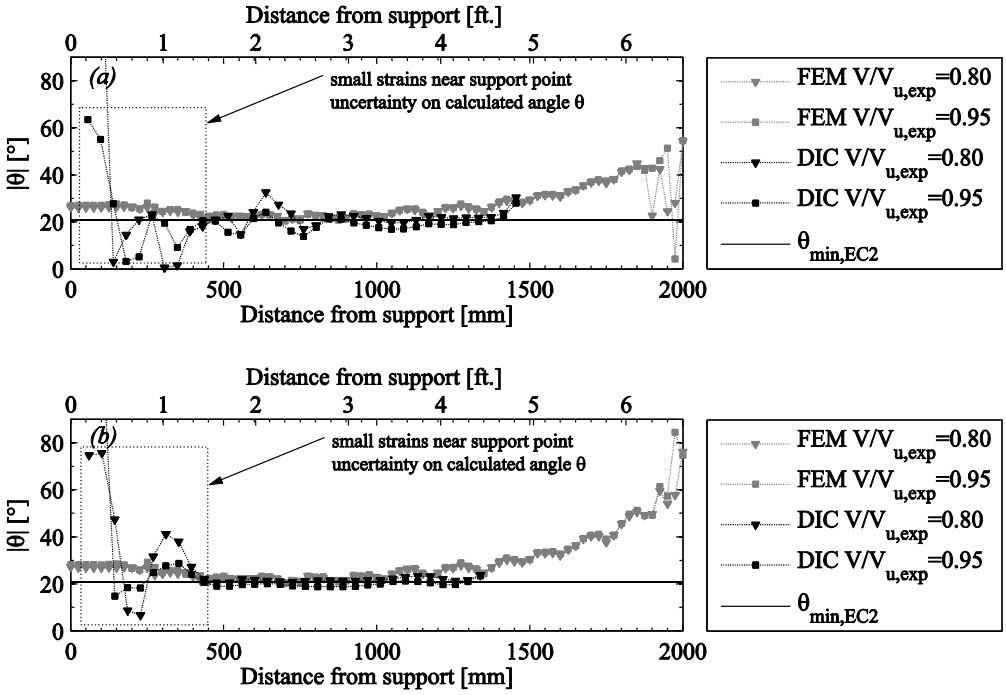

Fig. 8. Comparison between experimentally observed, numerically predicted and analytically calculated [2, 13] angle θ for specimen B104 as a function of the applied load and horizontal position at (a) 382mm (15.0 in.) and (b) 272mm (10.7 in.) from the bottom of the beam

From both Fig 8(a)-(b), a satisfying correlation is found between the experimentally observed, numerically predicted and analytically calculated angle θ. Close to the support point, small strain values are expected. Therefore, certain noise on the calculated angle is to be dealt with in that zone. Similar results were found for other specimens. Since EC2 states that the provided amount of shear reinforcement must be solely able to resist the applied shear force, refer to Eq. (1), and no significant difference between the experimentally observed and analytically calculated angle θ is found, it can be concluded that important shear carrying mechanisms are being overlooked in the shear strength provisions of EC2. Therefore, the various shear force contributions are identified for each specimen at various load levels based on the output of the numerical model.

The numerically predicted shear stresses τ_{xy} will, if integrated over the element surface on which they act, resist the applied shear force. The contributions of the top (refer to Fig. 2(c), area ranging from z=630mm to z=470mm) and bottom flanges (area ranging from z=0mm to z=170mm) and the web (area ranging from z=170mm to z=470mm) can thus be determined as a function of the applied load and distance from the support point. Fig. 9(a)-(c) show the results for specimen B102. Similar results were found for the other reported test specimens. From Fig. 9(b)-(c), it can be concluded that a significant portion of the applied shear force is carried in both uncracked flanges after the occurrence of diagonal cracks. This shear force distribution seems not to differ greatly for increasing load.

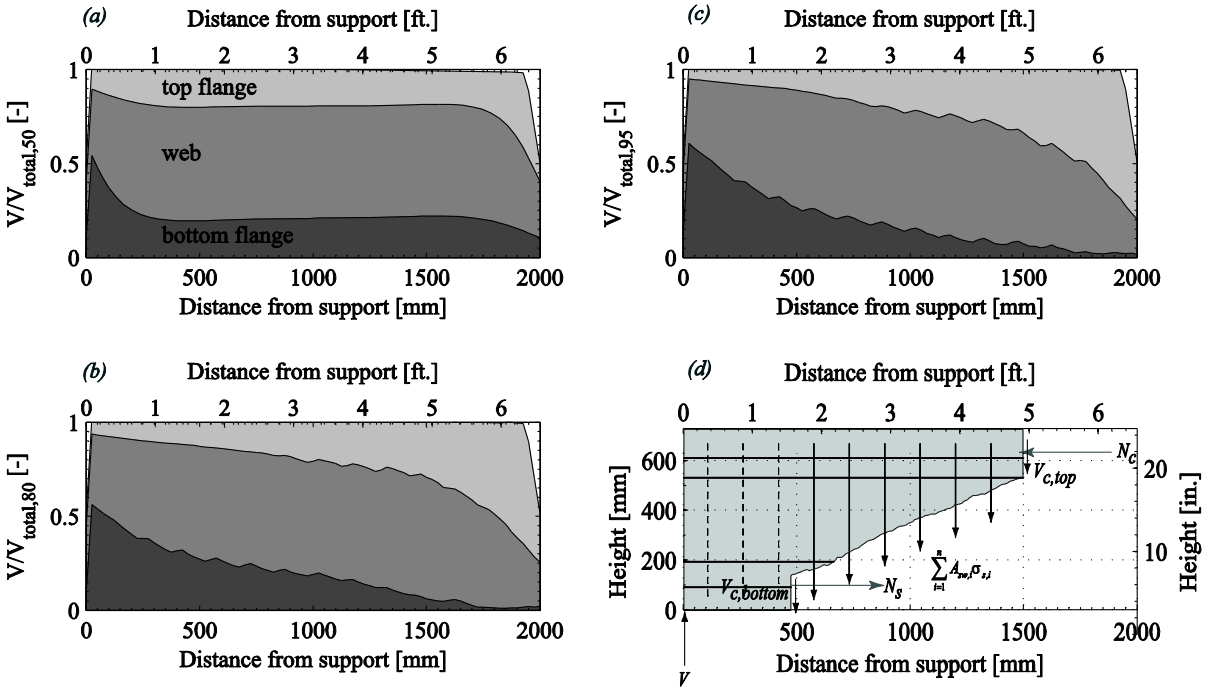

Fig. 9. Numerically predicted shear force contributions of top (light grey) and bottom (dark grey) flanges and web of specimen B102: (a) 50% of $V_{u,exp}$; (b) 80% of $V_{u,exp}$; (c) 95% of $V_{u,exp}$; (d) crack-based free-body (CBFB) diagram of specimen B102 with identified shear force contributions

Fig. 9(d) depicts a crack-based free-body (CBFB) diagram of specimen B102. It is assumed that only the shear reinforcement crossing the critical shear crack (i.e. the crack where failure is initiated) as well as the identified shear forces carried in both flanges contribute to the overall shear force equilibrium. The influence of aggregate interlock and dowel action is not taken into account. Since high strength concrete, leading to relatively smooth crack surfaces, is used and relatively large crack openings occur near failure, the possibility of generating shear stresses on the crack face is severely limited. Neglecting dowel action is justified since the 7-wire strands used for each specimen are characterized by a low transversal stiffness.

From Fig. 9(d), it can be seen that six stirrups cross the crack opening of specimen B102. Using the material properties reported in Table 2 and assuming that the stress in each stirrup reaches the ultimate tensile strength, a total of 107.9kN (24.3 kip) (i.e. 33.5% of the experimentally observed failure load of specimen B102). From Fig. 9(b)-(c), it can be seen that approximately 32% and 31% of the applied shear force is carried in the upper respectively lower uncracked flange. It can be concluded that a good prediction of the actual shear capacity is obtained if the shear force contributions found in the upper and lower flanges are taken into account.

CONCLUSIONS

This paper presents the results of six prestressed concrete I-shaped beams subjected to a four-point bending test until failure. During four of the six tests, two stereo-vision digital image correlation (DIC) systems were used to continuously measure full-field displacements and deformations. The experimental data were used to validate nonlinear finite element models constructed within the commercially available software package ANSYS v14. A good correlation was found between the experimentally observed and numerically predicted values concerning failure load, failure mode and displacements. Based on the numerical output, it was found that the analytical model which forms the basis for the shear strength provisions found in EC2, does not capture the actual structural behaviour of the reported test specimens. Therefore, an investigation of the shear carrying mechanisms is made as a function of the applied load and distance from the support point. It was found that a significant portion of the applied load is carried in the top and bottom flanges. If these shear force contributions are taken into account, better analytical predictions of the shear capacity are found.

REFERENCES

1. Ritter, W., *Die Bauweise Hennebique.* Schweizerische Bauzeitung, 1899. **33**: p. 41-61.
2. CEN, *Eurocode 2: Design of concrete structures - Part 1-1: General rules and rules for buildings*, 2004, NBN: Brussels. p. 255.
3. ACI, *ACI 318-11 Biulding Code Requirements for Structural Concrete and Commentary*, 2011, American Concrete Insitute: Farmington Hills, Mich. (USA). p. 503.
4. CSA, *CSA A23.3 Design of Concrete Structures (CSA A23.3-04)*, 2004, Canadian Standards Association: Mississauga p. 230.
5. Schlaich, J., K. Schafer, and M. Jennewein, *Toward a Consistent Design of Structural Concrete.* Journal Prestressed Concrete Institute, 1987. **32**(3): p. 74-150.
6. Muttoni, A., J. Schwartz, and B. Thurlimann, *Design of Concrete Structures with Stress Fields*. 1997: Birkhaüser/Springer. 145pp.
7. Muttoni, A. and M.F. Ruiz, *Shear strength of members without transverse reinforcement as function of critical shear crack width.* Aci Structural Journal, 2008. **105**(2): p. 163-172.
8. Ruiz, M.F. and A. Muttoni, *Applications of Critical Shear Crack Theory to Punching of Reinforced Concrete Slabs with Transverse Reinforcement.* Aci Structural Journal, 2009. **106**(4): p. 485-494.
9. Vecchio, F.J. and M.P. Collins, *The Modified Compression-Field Theory for Reinforced-Concrete Elements Subjected to Shear.* Journal of the American Concrete Institute, 1986. **83**(2): p. 219-231.
10. Vecchio, F.J., *Disturbed stress field model for reinforced concrete: Implementation.* Journal of Structural Engineering-Asce, 2001. **127**(1): p. 12-20.
11. Pang, X.B.D. and T.T.C. Hsu, *Fixed angle softened truss model for reinforced concrete.* Aci Structural Journal, 1996. **93**(2): p. 197-207.

12. fib, *Shear and punching shear in RC and FRC elements: Workshop 15-16 October 2010, Salò (Italy)*, in *fib Technical Report*, V.M. Sigrist, F.; Plizzari, G.; Foster, S., Editor 2010, fib: Lausanne. p. 262.
13. NBN, *NBN EN 1992-1-1 ANB* in *Eurocode 2: Ontwerp en berekening van betonconstructies - Deel 1-1: Algemene regels en regels voor gebouwen (in Dutch) - National Application Document*2010, NBN National Bureau for Normalisation: Brussels. p. 32 pp.
14. Cooreman, S., et al., *Identification of the mechanical material parameters through inverse modelling.* Emerging Technologies in Non-Destructive Testing, 2008: p. 337-342.
15. Cooreman, S., et al., *Elasto-plastic material parameter identification by inverse methods: Calculation of the sensitivity matrix.* International Journal of Solids and Structures, 2007. **44**(13): p. 4329-4341.
16. Sas, G., et al., *Photographic strain monitoring during full-scale failure testing of Ornskoldsvik bridge.* Structural Health Monitoring-an International Journal, 2012. **11**(4): p. 489-498.
17. Ivanov, D., et al., *Strain mapping analysis of textile composites.* Optics and Lasers in Engineering, 2009. **47**(3-4): p. 360-370.
18. Lecompte, D.C., S.; Coppieters, S.; Vantomme, J.; Sol, H.; Debruyne, D., *Parameter identification for anisotropic plasticity model using digital image correlation: Comparison between uni-axial and bi-axial tensile testing.* European Journal of Computational Mechanics, 2009. **18**: p. 393-418.
19. Van Paepegem, W., et al., *Study of the deformation characteristics of window security film by digital image correlation techniques.* Optics and Lasers in Engineering, 2009. **47**(3-4): p. 390-397.
20. Lava, P., et al., *Assessment of measuring errors in DIC using deformation fields generated by plastic FEA.* Optics and Lasers in Engineering, 2009. **47**(7-8): p. 747-753.
21. De Wilder, K., et al., *Analysis of the structural behaviour of shear-critical and reinforced concrete beams using digital image correlation*, in *5th International Conference on Structural Engineering, Mechanics and Computations (SEMC2013)*, A. Zingoni, Editor 2013, Balkema: Cape Town, South Africa.
22. Lava, P., S. Cooreman, and D. Debruyne, *Study of systematic errors in strain fields obtained via DIC using heterogeneous deformation generated by plastic FEA.* Optics and Lasers in Engineering, 2010. **48**(4): p. 457-468.
23. Willam, K. and E. Warnke, *Constitutive model for the triaxial behavior of concrete*, in *International Association for Bridge and Structural Engineering*1975, ISMES: Bergamo, Italy. p. 174-204.
24. Hsu, T., *Unified Theory of Reinforced Concrete*. 1993, Boca Raton, FL, USA: CRC Press.